



Apo-metallothionein-3 cooperatively forms tightly compact structures under physiological conditions

Received for publication, October 20, 2022, and in revised form, January 3, 2023. Published, Papers in Press, January 11, 2023.
<https://doi.org/10.1016/j.jbc.2023.102899>

Amelia T. Yuan¹, Natalie C. Korkola¹, and Martin J. Stillman^{1*}

From the Department of Chemistry, University of Western Ontario, London, Ontario, Canada

Edited by Karen Fleming

Metallothioneins (MTs) are essential mammalian metal chaperones. MT isoform 1 (MT1) is expressed in the kidneys and isoform 3 (MT3) is expressed in nervous tissue. For MTs, the solution-based NMR structure was determined for metal-bound MT1 and MT2, and only one X-ray diffraction structure on a crystallized mixed metal-bound MT2 has been reported. The structure of solution-based metalated MT3 is partially known using NMR methods; however, little is known about the fluxional *de novo* apo-MT3 because the structure cannot be determined by traditional methods. Here, we used cysteine modification coupled with electrospray ionization mass spectrometry, denaturing reactions with guanidinium chloride, stopped-flow methods measuring cysteine modification and metalation, and ion mobility mass spectrometry to reveal that apo-MT3 adopts a compact structure under physiological conditions and an extended structure under denaturing conditions, with no intermediates. Compared with apo-MT1, we found that this compact apo-MT3 binds to a cysteine modifier more cooperatively at equilibrium and 0.5 times the rate, providing quantitative evidence that many of the 20 cysteines of apo-MT3 are less accessible than those of apo-MT1. In addition, this compact apo-MT3 can be identified as a distinct population using ion mobility mass spectrometry. Furthermore, proposed structural models can be calculated using molecular dynamics methods. Collectively, these findings provide support for MT3 acting as a noninducible regulator of the nervous system compared with MT1 as an inducible scavenger of trace metals and toxic metals in the kidneys.

In Nature, metalloproteins consist of approximately 30% of all proteins (1). These specialized proteins use the chemical properties of metal cofactors to catalyze reactions, participate in cell signaling, and stabilize structures (2–4). Among many physiologically essential metals in mammals are Zn^{2+} , $Fe^{2+/3+}$, and Cu^{+2+} . The regulation of these metals is crucial to the overall homeostatic stability of an organism.

There are many regulators of metals within a cellular environment, including metal transporters, metal influx and efflux pumps, and metal chaperones. An important metal chaperone is the protein metallothionein (MT) (5). Present across species, MTs play a crucial role in Cu^+ and Zn^{2+}

homeostasis, as well as in toxic metal sequestration (5). Mammalian MTs have 20 reduced cysteines but no disulfide bonds. The cysteine thiols instead bind metals ranging from Zn^{2+} (most common), Cd^{2+} , Cu^+ , as well as the xenobiotic metals of metallodrugs such as Pt^{2+} (6, 7). The fully metalated structure of mammalian MTs has two metal-binding domains: a C-terminal α domain consisting of 11 cysteines that bind to 4 divalent metals and an N-terminal β domain consisting of nine cysteines that bind to 3 divalent metals (6, 8–10). There are four isoforms of MTs within the human genome (11). Isoforms 1 (MT1) and 2 (MT2) are expressed in all tissues of the body, concentrating in the kidneys and liver, respectively. MT1 has been studied in the past as a “sink” for metal ions in the kidney. Isoform 3 (MT3) is mostly expressed in nervous tissue (12). Isoform 4 (MT4) is expressed in epithelial tissue.

MT3 is currently the most heavily researched MT due to its role in the progression of neurodegenerative diseases such as Alzheimer’s and Parkinson’s disease (12–15). In particular, MT3 acts as a neuronal growth inhibitory factor (15–17).

Although the two-domain structure of fully metalated mammalian MTs is well established from NMR spectroscopic studies and a single X-ray diffraction study of mixed-metal rat MT, the structures of metal-free apo-MTs remain largely unknown due to their flexibility and inaccessibility to traditional protein structural determination methods (8–10, 18). Initially, apo-MTs were thought to have little physiological relevance. However, in 2001, Yang *et al.* reported high levels of apo-MT present in the liver, brain, and kidneys of rats using fluorescence labeling (19). Their report emphasized the importance of studying the stability and the early stages of metalation of apo-MTs (20). Apo-MTs were initially defined as intrinsically disordered proteins (IDPs), with no defined structures. However, molecular dynamics methods show that apo-MTs retain much of their structure in the absence of metals at physiological pH, despite not having traditional formal structure based on secondary structural elements such as α helices or β pleated sheets (21). The charge states from electrospray ionization mass spectral (ESI-MS) studies, which are sensitive to the overall surface area of the protein, also showed little change as apo-MT was metalated, indicating that the apo-MT structure was not significantly altered following metalation (22, 23).

* For correspondence: Martin J. Stillman, martin.stillman@uwo.ca.

Apo-metallothionein-3 cooperatively forms compact structures

MT3 has been reported to have strikingly different metalation properties compared with the other isoforms (12, 13, 15, 24–28). However, the structural properties of apo-MT3 have not been reported to date.

In this article, we reveal that, although no formal structures are present, apo-MT3 exists as an unusually compact structure under physiological conditions. Methods used to support our analysis include ESI-MS, cysteine modification using N-ethylmaleimide (NEM), and ion mobility mass spectrometry (IM-MS). We use the denaturing agent guanidinium chloride (GdmCl) and low pH conditions to evaluate the properties of its compact conformation. Our use of NEM to selectively modify cysteinyl thiols is similar to the use of hydrogen–deuterium exchange to probe structural properties of formally folded proteins. We report that two distinct conformational populations of apo-MT3 exist: a compact conformation under physiological conditions and an extended conformation under denaturing conditions, with minimal intermediate structures detected. This switch in conformation is distinct from IDPs that exist as a continuum of conformations. A compact conformation of apo-MT3 may be a necessary adaptation to protect its cysteines from oxidation *in vivo* and support its role as a regulator of neurological function.

Results

ESI-mass spectral data of apo-MT3 cysteine modification

In all experiments, the MTs were fully reduced with the use of evacuation followed by argon saturation. The UV-visible absorption spectra of aliquots of the protein samples were recorded prior to the measurement to ensure 280 nm absorption characteristic of disulfide bond formation was not present. The amino acid sequence of the recombinant apo-MT3 used is described in Figure 1, with yellow highlighting the 20 cysteines and the metal-induced domains labeled. We show the data for cysteine modification of apo-MT3 at pH 7.4, 5.0, and 2.9 in Figure 2. Figure 2*i* shows the charge state and deconvoluted cysteine modification profile of apo-MT3 at physiological pH (pH 7.4). The mass spectral data follow the stepwise addition of the cysteine modifier NEM (125 Da) at 0, 1.9, 10.3, 20 molar equivalents (mol. eq.) to apo-MT3 (8212 Da). The data are representative of a cooperative modification pattern, where the stepwise addition of NEM results initially in solely apo-MT3 and NEM₂₀MT3 species. Significantly, NEM_n-MT3 species (n = 1–19) are not present. We described this as a cooperative profile because the reaction of the first NEM molecule to a cohort of apo-MT3 triggers the subsequent reaction of the next 19 NEM molecules to the

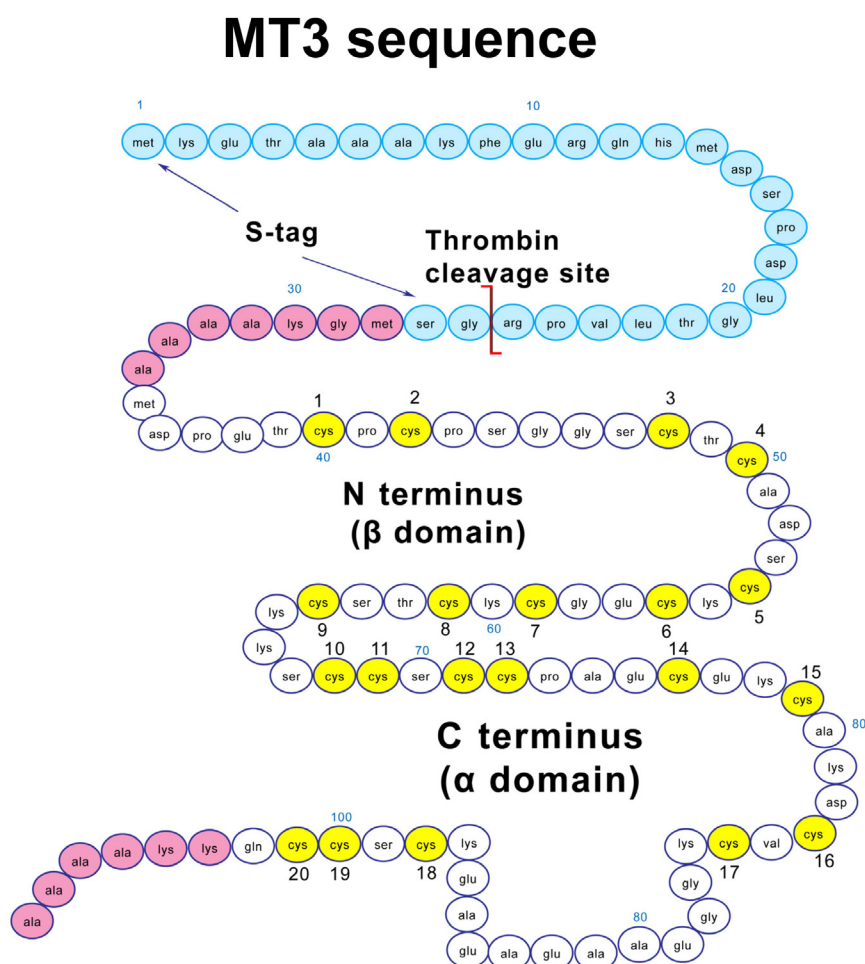


Figure 1. Amino acid sequence for apo-MT3. Amino acids (AAs) 35 to 64 form the β domain, 65 to 67 form the linker region, and 68 to 102 form the α domain. The domains are labeled for the clusters formed when divalent metals bind to the cysteines (yellow). The AAs in pink are included in the recombinant protein for stability. The AAs in blue are the S-tag for increased stability, removed in the protein purification process.

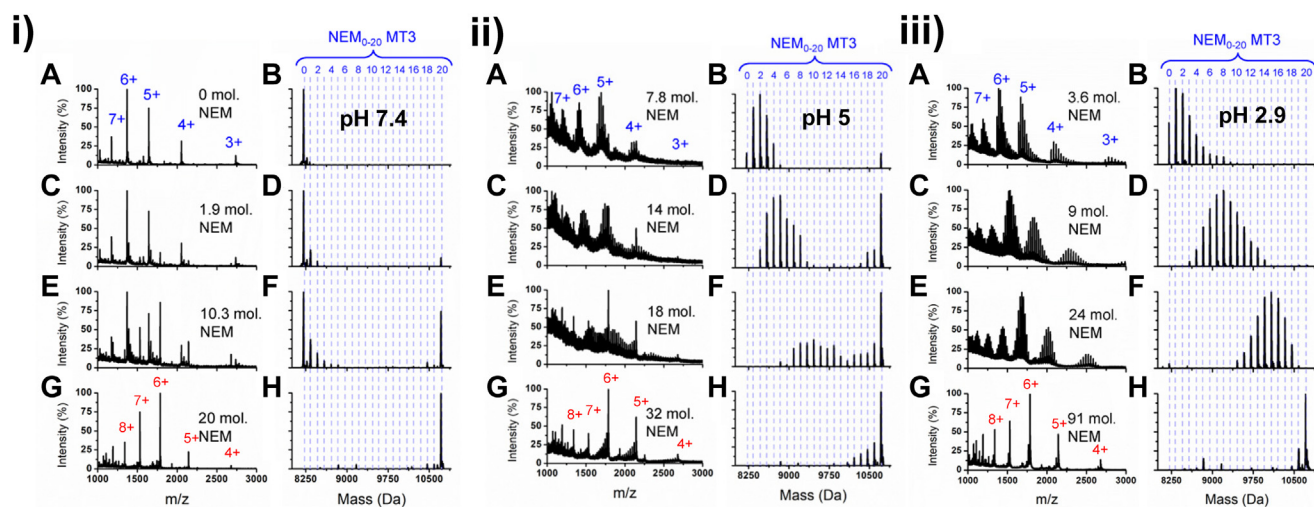


Figure 2. i) Sequential modification of apo-MT3 by NEM at pH 7.4. A, C, E, and G show the charge state spectra recorded with increasing (0, 1.9, 10.3, 20) mol. eq. of NEM added. The charge states for the apo protein are labeled in A, and the charge states for the fully modified protein are labeled in G. B, D, F, and H show the corresponding deconvoluted spectra. The mass of apo-MT3 is 8212 Da, and a single NEM modification adds 125 Da. The separation of the increasing NEM modifications is indicated by the dotted lines at 125 Da intervals. The modifications shown range from 1 to 20 NEM bound for the 20 cysteines of MT3. ii) Mixture of normal distribution and cooperative profiles for apo-MT3 when modified by NEM at pH 5.0. A, C, E, and G show the charge state spectra recorded with increasing (7.8, 14, 18, 32) mol. eq. of NEM added. B, D, F, and H show the corresponding deconvoluted spectra. The mass of apo-MT3 is 8212 Da, and a single NEM modification adds 125 Da. The separation of the increasing NEM modifications is indicated by the dotted lines at 125 Da intervals. The modifications shown range from 1 to 20 NEM bound for the 20 cysteines of MT3. iii) Normal distribution of modified cysteines for apo-MT3 when modified by NEM at pH 2.9. A, C, E, and G show the charge state spectra recorded with increasing (3.6, 9, 24, 91) mol. eq. of NEM added. NEM, N-ethylmaleimide. B, D, F, and H show the corresponding deconvoluted spectra. The mass of apo-MT3 is 8212 Da, and a single NEM modification adds 125 Da. The separation of the increasing NEM modifications is indicated by the dotted lines at 125 Da intervals. The modifications shown range from 1 to 20 NEM bound for the 20 cysteines of MT3. NEM, N-ethylmaleimide.

same set of MT3 proteins, resulting in the entire protein being modified to completion.

In contrast, when the NEM modification was carried out at pH 2.9, the ESI mass spectral data recorded is noncooperative (Fig. 2iii). Stepwise addition of NEM at 3.6, 9, 24, and 91 mol. eq. results in a Normal binomial distribution of modified protein species centered on the mass of the average number of NEM bound. Excess NEM is required to drive the reaction to completion at acidic pH due to the competition from cysteine protonation. The Normal distribution of NEM modifications indicates that the cysteines are equally accessible to the NEM modifier, resulting in a noncooperative profile based solely on the statistical availability of the cysteinyl thiols.

The mass spectral data for the stepwise titration of NEM into apo-MT3 at pH 5 represents a mixture of both cooperative and noncooperative profiles (Fig. 2ii). NEM was added with 7.8, 14, 18, and 32 mol. eq. to apo-MT3 at pH 5. Figure 2iiB shows that, with 7.8 mol. eq. of NEM added, there is simultaneously a small fraction of fully modified NEM₂₀MT3 with a large fraction of partially modified MT3 (NEM₁₋₅MT3). This trend continues as more NEM is added so that in panel D, both the Normal distribution of peaks centered on NEM₄MT3 and the cooperatively formed NEM₂₀MT3 are present.

ESI-mass spectral data of apo-MT1 cysteine modification

Figure 3i shows the NEM modification profile of apo-MT1 at pH 7.4 from a stepwise titration monitored by ESI-MS. A more complicated semi-cooperative profile is recorded where both apo-MT1 and NEM₂₀MT1 are present in addition to

varying amounts of other NEM-modified species. Specifically, a Normal distribution is formed in the earlier steps of the titrations in addition to the formation of NEM₂₀MT1. Interestingly, with just 5 mol. eq. of NEM added, small amounts of NEM₇MT1 to NEM₁₉MT1 are formed that do not follow a Normal distribution. However, with 8 mol. eq. of NEM added (Fig. 3iF), the profile closely resembles the pH 5 data of MT3 (Fig. 2iiD).

Figure 3ii shows the NEM modification profile of apo-MT1 at pH 5 through a stepwise titration monitored by ESI-MS. The data indicate a completely noncooperative profile where the Normal distribution is centered on the stoichiometric amount of NEM added. The observed modification profile indicates that all cysteines of apo-MT1 are completely exposed at pH 5, where the profiles closely resemble that of MT3 at pH 2.9 (Fig. 2iii).

Denaturation effects on the cysteine modification reaction

The compact apo-MT3 structure was further investigated by introducing increasing concentrations of the denaturing agent, GdmCl (Fig. 3). We have previously reported that 3 M GdmCl denatures apo-MT1 completely (29). Using apo-MT1 as a guide, we can interpret the results from the reactions of GdmCl with apo-MT3. Apo-MT3 was equilibrated in increasing concentrations of GdmCl (0–4 M) before adding 10 mol. eq. of NEM to determine the level of denaturation. The resulting ESI-mass spectral data are shown in Figure 4. Even with GdmCl concentrations up to 4 M, there is little to no change in the distribution of NEM-modified species, and the distribution remains cooperative, with only apo-MT3 and

Apo-metallothionein-3 cooperatively forms compact structures

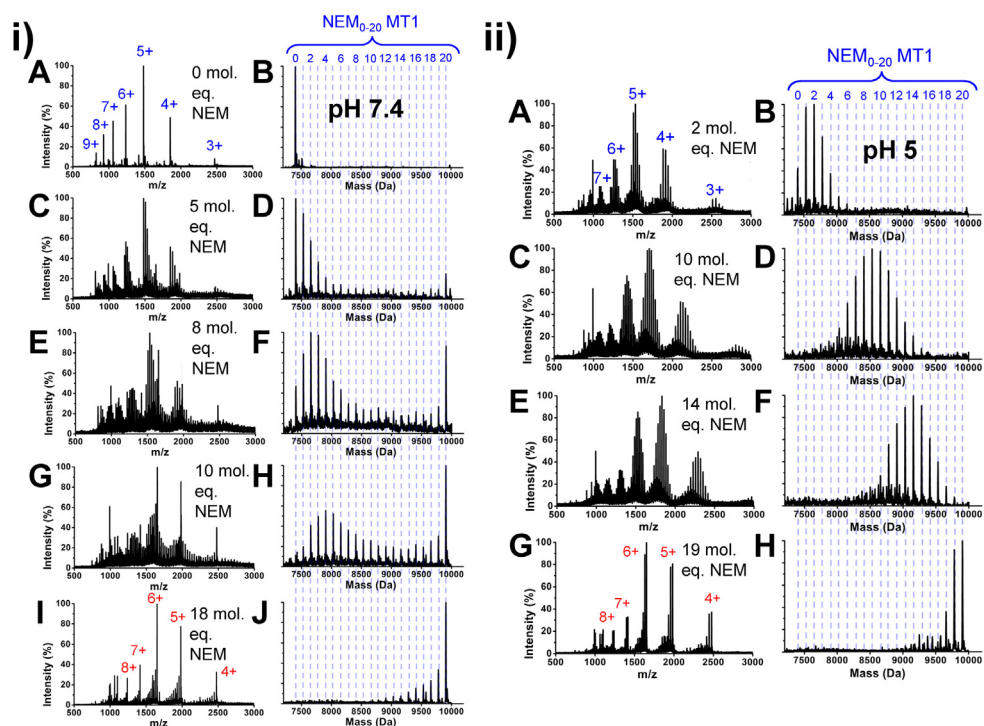


Figure 3. Dependence on pH of the NEM cysteine modification profiles for apo-MT1. (i) Sequential modification of apo-MT1 by NEM at pH 7.4 monitored by electrospray ionization mass spectrometry showing additions of 0, 5, 8, 10, and 18 mol. eq. NEM. A, C, E, G, and I show the charge state spectra with labeled charge states in A (for the unmodified protein) and I (for the fully modified protein), and B, D, F, H, and J show the associated deconvoluted spectra. The mass of apo-MT1 is 7404 Da, and a single NEM modification adds 125 Da. The separation of the increasing NEM modifications is indicated by the dotted lines at 125 Da intervals. The modifications shown range from 1 to 20 NEM bound for the 20 cysteines of MT1. (ii) A stepwise titration of NEM into apo-MT1 at pH 5 monitored by electrospray ionization mass spectrometry showing additions of 2, 10, 14, and 19 mol. eq. NEM. A, C, E, and G show the charge state spectra with labeled charge states in A (for the protein with 2 mol. Eq. NEM added) and G (for the fully modified protein), and B, D, F, and H show the associated deconvoluted spectra. The mass of apo-MT1 is 7404 Da, and a single NEM modification adds 125 Da. The separation of the increasing NEM modifications is indicated by the dotted lines at 125 Da intervals. The modifications shown range from 1 to 20 NEM bound for the 20 cysteines of MT1. Charge states for the unmodified protein are shown in blue, and charge states for the fully modified protein are shown in red. NEM, N-ethylmaleimide.

NEM₂₀MT3 as the dominant species. This is a vastly different outcome from the modification patterns reported previously for apo-MT1 and indicates that the addition of the 4 M GdmCl did not result in greater exposure of the 20 cysteines in apo-MT3 (29).

NEM modification reaction rates for apo-MT3 and apo-MT1

Using stopped flow kinetics, we measured the rate of the decrease in free NEM concentration as it reacted with the cysteines of the apo-MTs. The rate of cysteine modification has been previously used with other proteins to determine whether the conformation was folded (slow rate) or unfolded (fast rate) (30). Using the NEM extinction coefficient of $\epsilon_{300\text{ nm}} = 620\text{ M}^{-1}\text{ cm}^{-1}$, the rate of reduction in the absorbance of the free NEM was determined (Fig. 5i) (31–34). The data in Figure 5i compare the rate of reaction of NEM with the cysteines of apo-MT1 (Fig. 5iA) and apo-MT3 (Fig. 5iB). In Figure 5iA, the data show that the apo-MT1 binds to excess NEM with a rate constant of $7500 \pm 25\text{ M}^{-1}\text{ s}^{-1}$, whereas in Figure 5iB, the apo-MT3 cysteines react significantly slower with NEM with a rate constant of $3834 \pm 3\text{ M}^{-1}\text{ s}^{-1}$. Triplicates were completed to ensure precision. There is a significant difference ($p < 0.001$) between the rates of modification of the two apo proteins. In Figure 5iC, the fitted traces were normalized to have the same exact start

and end points for MT1 and MT3: the difference in the rates of modification is clear. For similar proteins with 70% homology, this 2-fold difference in rate of modification is significant.

Further analysis of apo-MT1 and apo-MT3 under 4 M GdmCl conditions was used to assess the rate of decrease of the free NEM signal at 300 nm (Fig. S1). Although we expected the NEM to be depleted at a faster rate with the denaturation of apo-MT1, an overall decrease in modification rates was seen for both apo-MT1 and apo-MT3. However, the same pattern remains for the comparison between apo-MT1 and MT3 whereby, in the presence of GdmCl, apo-MT1 still reduces the free NEM signal at a faster rate than apo-MT3 indicating that modification of the cysteines is faster in apo-MT1 than in apo-MT3.

In contrast to the direct modification reaction of apo-MTs with NEM, which monitors the accessibility of the cysteines, we measured the metalation kinetics, which monitors the accessibility of the cysteines to form Cd-S bonds. Metalthiolate clusters are formed by multiple cysteines for MTs, with 11 cysteines forming a 4 divalent metal cluster (Cd₄S₁₁) and 9 cysteines forming a 3 divalent metal cluster (Cd₃S₉) (6). Cd²⁺ ions bind to the cysteines of MTs with a tetrahedral geometry involving four cysteines (35). When the Cd²⁺ is added above 5 mol. eq., cluster formation takes place. Owing

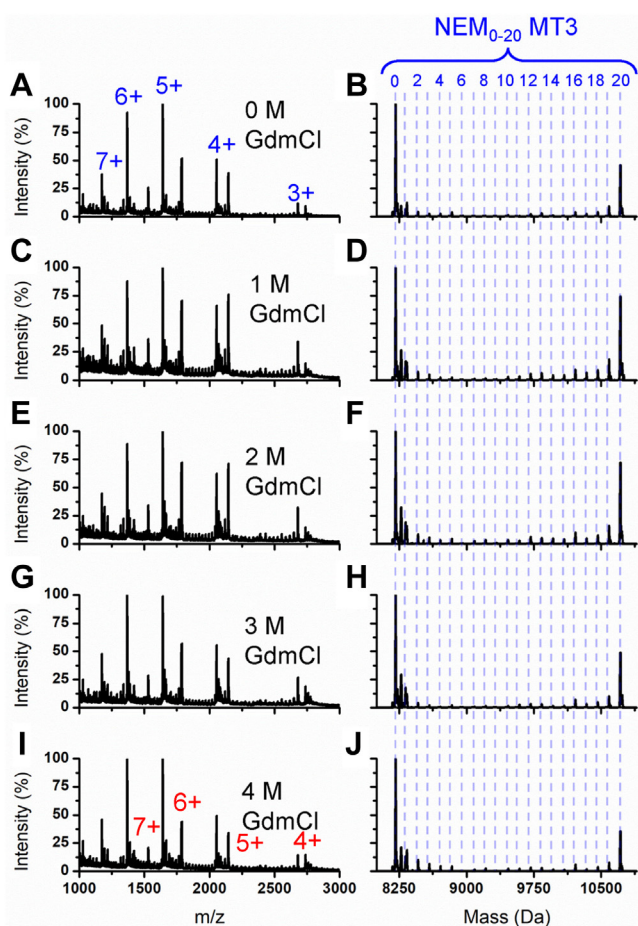


Figure 4. Dependence on GdmCl concentration of the NEM cysteine modification profiles for apo-MT3. NEM modification of apo-MT3 by NEM at pH 7.4 with varying amounts of GdmCl. In each titration experiment, 10 mol. eq. of NEM was added. A, C, E, G, and I show the charge state spectra recorded with 0, 1, 2, 3, 4 M GdmCl added to the solutions. The charge states are labeled in A for the unmodified protein and I for the fully modified protein and apply to each panel in the column. The charge states labeled are for both apo-MT3 and NEM₂₀MT3. B, D, F, H, and J show the deconvoluted spectra. The mass of apo-MT3 is 8210 Da, and a single NEM modification adds 125 Da. The separation of the increasing NEM modifications is indicated by the dotted lines at 125 Da intervals. The modifications shown range from 1 to 20 NEM bound for the 20 cysteines of MT3. GdmCl, guanidinium chloride; NEM, N-ethylmaleimide.

to the multiple cysteines required to form such as cluster, clusters form faster if the protein is compact due to the proximity of the cysteines and ability to realign rapidly (29).

In Figure 5ii, the stopped flow kinetic traces are recorded for the formation of Cd₇MT from the reduced apo-MT1 (panel A) and apo-MT3 (panel B) with 7 mol. eq. of Cd(OAc)₂. The fitted rate constant for apo-MT1 is $348 \pm 6 \times 10^5 \text{ M}^{-1} \text{ s}^{-1}$, and the fitted rate constant for apo-MT3 is $582 \pm 11 \times 10^5 \text{ M}^{-1} \text{ s}^{-1}$. These values are significantly different ($p < 0.001$). Triplicates were completed to ensure accuracy and precision. In addition to carrying out the metalation under physiological conditions, 4 M GdmCl conditions were also studied (panel C, apo-MT1; panel D, apo-MT3). The metalation reactions in the presence of GdmCl were analyzed using the same concentrations of reactants as for the reaction shown in Figure 5i. The fitted rate constant for apo-MT1 in 4 M GdmCl is $252 \pm 2 \times 10^5 \text{ M}^{-1} \text{ s}^{-1}$,

and the fitted rate constant for apo-MT3 in 4 M GdmCl is $343 \pm 3 \times 10^5 \text{ M}^{-1} \text{ s}^{-1}$. In Figure 5ii, E and F, we show the fitted traces normalized to have the same exact start and end points for MT1 and MT3: the difference in the rates of metalation is clear with the same trend as in the absence of GdmCl, where apo-MT1 metalates slower than apo-MT3.

Structure determination of apo-MT3 using IM-MS

IM-MS was used to provide direct structural information about the relative size of apo-MT3. IM-MS has previously been used to determine the overall conformational size of proteins, using drift time and subsequently calculated collision cross section (CCS) measurements (36–40). The CCS calibration was performed according to the protocol developed by Ruotolo *et al* (41). Figure 6 shows the CCS profiles of the 7+ charge state of apo-MT3 at pH 7.4, 5.0, and 2.2 (panels A, B, C). The dotted lines show the maxima of the CCS for the compact conformation (1192 Å²) and the larger expanded conformation (1356 Å²). This is within the CCS range of MT2 reported by Chen and Russell, although they measured a different charge state (41, 42). The compact conformation travels faster through the IM-MS cell because of its lower surface area to volume ratio, allowing greater mobility through the IM-MS gas (N₂). The relative intensity of the compact and expanded conformations can be monitored (panel D) and the ratio of compact to extended protein can be calculated (panel E). Although we expected to see only a compact structure at pH 7.4 and extended structure at pH 2.2 based on the data shown in Figure 2, full separation of the two conformations was not complete (Fig. 6, A/C). The IM-MS parameters were adjusted to be as soft as possible to avoid conformational change as best as possible (36, 41, 42). Other charge states of the apo-MT3 under all conditions were analyzed; however, the distinct conformational populations were not resolved; to demonstrate, the drift time spectra for the 5+ and 10+ charge states on both extremes are shown in Fig. S2.

Apo-MT3 structure calculations using molecular dynamics

Structural models of apo-MT3 were calculated using molecular mechanics and molecular dynamics methods (Fig. 7i). Starting structures for the apo-MT3 model were generated with the input of the protein sequence. Compact conformations of apo-MT3 were modeled using 300 K temperature settings to allow for hydrogen bond formation. Because hydrogen bonds are weak and related to the distance between the electronegative ion and the electropositive proton, we can mimic the effect of hydrogen bond formation using low temperatures to allow for hydrogen bond-driven stabilization of structures. In contrast, expanded conformations of apo-MT3 were modeled using 1000 K to mimic an environment unfavorable for hydrogen bond formation, such as under acidic pH. This is similar to the principles of heat denaturation (43). The calculated surface accessibility of the expanded structure using the 1000 K apo-MT3 (9753 Å²) minimized geometry is greater than that of the 300 K apo-MT3 structure (4544 Å²) (44).

Apo-metallothionein-3 cooperatively forms compact structures

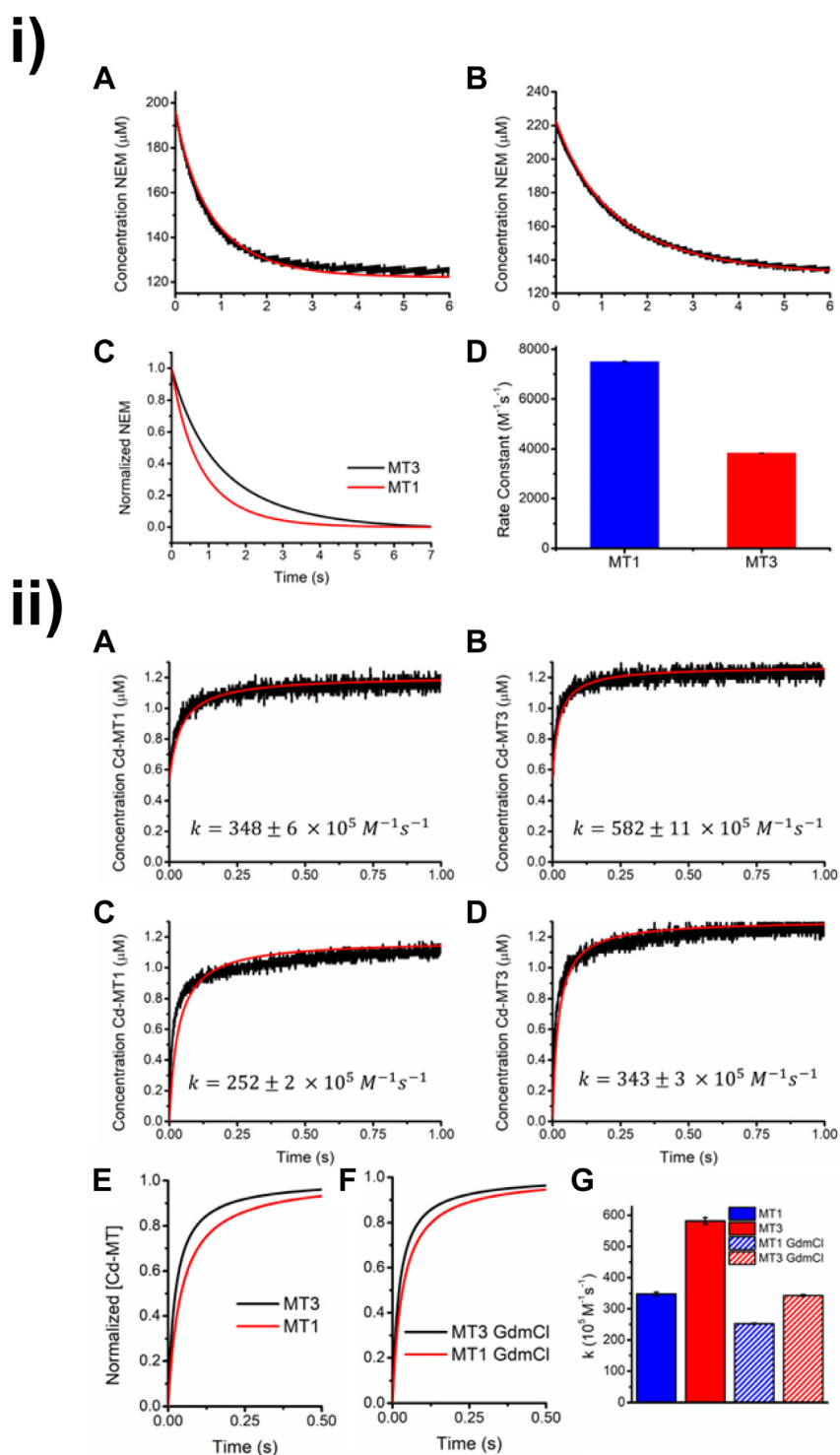


Figure 5. i) Fitted kinetic traces recorded for the reaction of 5 μM (A) apo-MT1 and (B) apo-MT3 with 200 μM (40 mol. eq.) NEM at pH 7.4 monitored at 300 nm. Reported k values were determined using triplicates. (C) normalized kinetics traces of A–B for visual comparison of the two isoforms' reaction rate. (D) bar graph representation of the rate constants obtained from the fitted line in (A and B). ii) Fitted kinetic traces recorded for the Cd^{2+} metalation of 1.25 μM (A) apo-MT1 in absence of GdmCl, (B) apo-MT3 in the absence of GdmCl, (C) apo-MT1 in the presence of 4 M GdmCl, and (D) apo-MT3 in the presence of 4 M GdmCl. The $\text{Cd}(\text{OAc})_2$ concentration was 8.75 μM (7 mol. eq.) at pH 7.4, and the reaction was monitored at 250 nm. (E) normalized kinetics traces of the metalation of MT1 and MT3 in the absence of GdmCl (A and B) and (F) the normalized kinetic traces of the metalation of MT1 and MT3 in the presence of GdmCl (C–D) for visual comparison of the two isoforms' metalation rates. (G) bar graph representation of the rate constants obtained from the fitted lines in (A–D). GdmCl, guanidinium chloride; NEM, N-ethylmaleimide.

Molecular dynamics calculations were also performed on partially modified and fully modified MT3 with NEM (Fig. 7ii). The structure from the 300 K molecular dynamics calculation was used, and the most exposed cysteines were modified with

NEM, 5 mol. eq. at a time (Fig. 7ii, A–E). The lowest energy conformations from each molecular dynamics calculation are shown in Figure 7ii. Stepwise modification results in the gradual exposure of additional unmodified cysteines (the

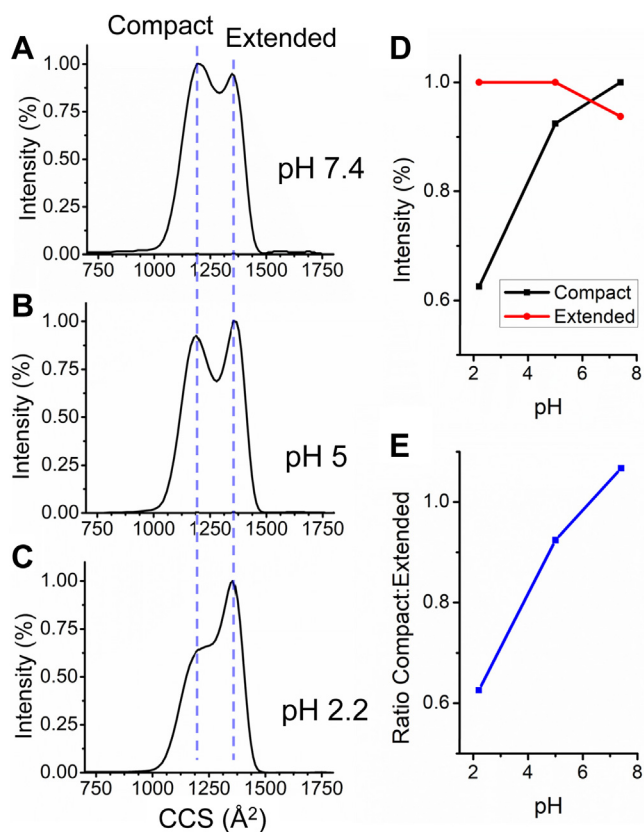


Figure 6. Ion mobility mass spectra collision cross sections (CCSs) for apo-MT3 at varying pH values. The compact conformation was determined to have a CCS of 1192 Å², and the extended conformation has a CCS of 1356 Å². A, B, and C show the CCS profile of the 7+ charge state of apo-MT3 at pH 7.4, 5.0, and 2.2, respectively. D shows the normalized intensity of the compact and extended conformations. E shows the ratio of the compact to extended conformations with respect to pH.

modified cysteines are shown in orange and the unmodified cysteines are shown in yellow); this models the behavior exhibited by apo-MT3 at pH 7.4 (Fig. 2I). Specifically, Cys64, Cys71, Cys79, Cys98, Cys101 were first modified by NEM as the most exposed cysteines from Figure 7iiA (apo-MT3). Subsequently, Cys48, Cys50, Cys54, Cys56, and Cys85 were modified as the exposed cysteines from Figure 7iiB (NEM₅MT3). After that, Cys42, Cys59, Cys61, Cys72, and Cys76 were modified as they became exposed on Figure 7iiC (NEM₁₀MT3). Lastly, Cys40, Cys68, Cys69, Cys83, and Cys100 were modified from the starting structure of Figure 7iiD (NEM₁₅MT3). The fully modified protein is shown in Figure 7iiE (NEM₂₀MT3). The cysteines modified for each step were chosen based on their proximity to the surface of the protein or their exposure to NEM.

In addition, molecular dynamics calculations were carried out for apo-MT1 for comparison. Calculations were performed starting from sequence input. The lowest potential energy geometries are shown in Figure 8 for apo-MT3 under 300 K conditions (Fig. 8A) and 1000 K (Fig. 8B). The calculated surface accessibility of the 300 and 1000 K structures was 6024 and 8960 Å², respectively (44).

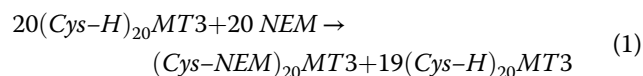
Discussion

NEM modification reveals compact conformation of apo-MT3 in comparison with apo-MT1

When analyzing the ESI-mass spectral data, it is important to note the charge state spectrum is related to the overall surface area of the sample (45, 46). Looking at Figure 2, i and iii, we see a shift from predominantly 6+ and 5+ charge states with low or no cysteinyl modification (panel A), to 7+ and 6+ charge states with an increase in NEM modification (panel G). We interpret the increase in the average charge state of the protein as resulting from the unfolding of the protein, as the peptide chain supports more charge. In other words, the starting apo-MT3 is more compact than the modified MT3.

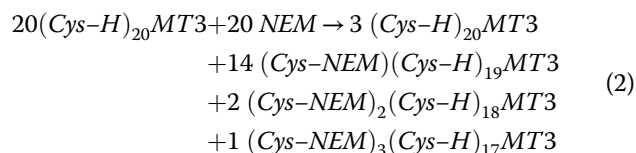
Next, we can compare the modification profiles shown in Figure 2, i and iii, which show cysteine modification of MT3 at pH 7.4 and 2.9, respectively.

If we consider adding 20 NEM to 20 apo-MT3 (1 mol. eq.), the cooperative mechanism can be stated as:



In this case, 1 MT3 molecule is modified to completion with all 20 cysteines bound to NEM while 19 MT3 molecules are unmodified.

If we consider a noncooperative mechanism, the statistical distribution following the reaction of 20 NEM to 20 apo-MT3 (1 mol. eq.) can be described as follows:



In this case, there is a Normal distribution of the species of modified MT3 centered on a mean of one NEM bound, which is (Cys-NEM)(Cys-H)₁₉MT3.

At pH 7.4, the major species that forms during the titration is the NEM₂₀MT3 with very low abundance of intermediate species. This supports our assessment that the reaction follows the cooperative pathway of Equation 1. In contrast, at pH 2.9, multiple intermediate species are observed, forming a Normal distribution that centers on the average NEM mol. eq. bound. In this case, the reaction follows the noncooperative pathway of Equation 2.

The Equation 1 pathway represents the reaction of the compact conformation where most cysteines are not accessible. Under these conditions, an NEM-modification reaction triggers the exposure of additional cysteines to modification. In contrast, the fully extended conformation allows equal access to all cysteines, which results in a Normal distribution of species centered on the average mol. eq. of NEM bound (Equation 2). Significantly, this means that there are two

Apo-metallothionein-3 cooperatively forms compact structures

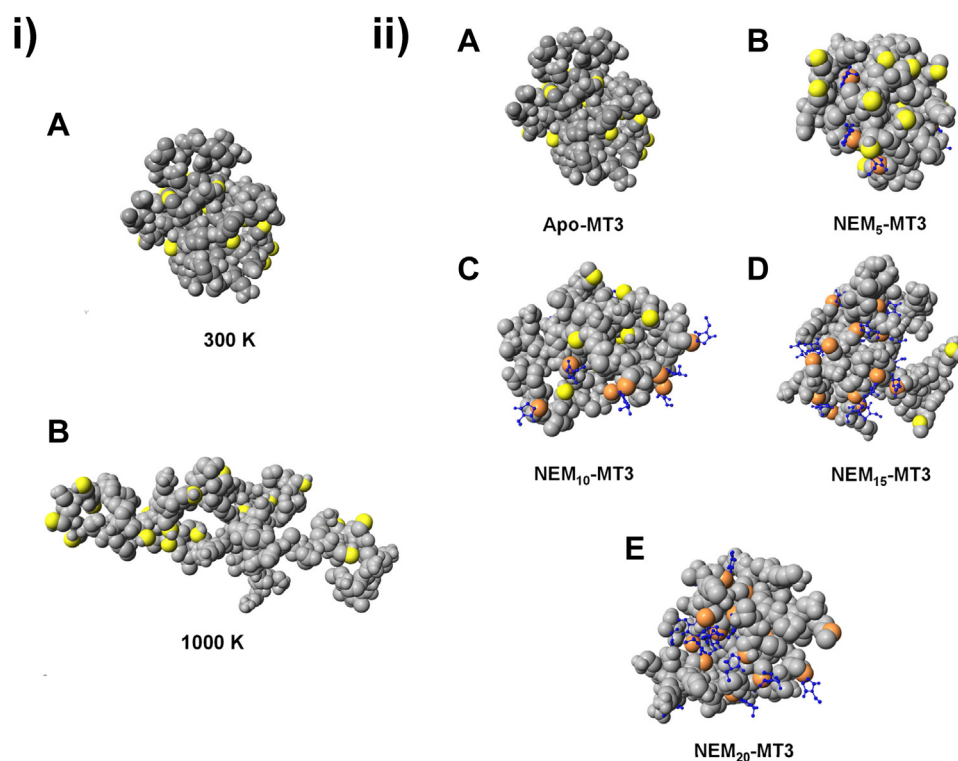


Figure 7. i) Calculated models of open conformation (A) and closed conformation (B) apo-MT3 using molecular mechanics and molecular dynamics methods. The *yellow* residues represent cysteines. (A) space-filling model of apo-MT3 calculated under 300 K conditions for 1000 ps with a 0.02-ps equilibration time. (B) space-filling model of apo-MT3 calculated under 1000 K conditions for 1000 ps with a 0.02-ps equilibration time. ii) Calculated models of stepwise modification of apo-MT3 with NEM using molecular mechanics and molecular dynamics methods. All models are calculated under 300 K conditions for 1000 ps with a 0.02-ps equilibration time. Unmodified cysteines are noted in yellow, and modified cysteines are in orange. NEM is noted in blue. The rest of the protein is noted in gray. (A) space-filling model of apo-MT3. (B) space-filling model of NEM₅-MT3. (C) space-filling model of NEM₁₀-MT3. (D) space-filling model of NEM₁₅-MT3. (E) space-filling model of NEM₂₀-MT3. NEM, N-ethylmaleimide.

distinct cohorts of apo-MT3 coexisting at pH 5 (Fig. 2ii): the compact cohort at pH 7.4 and the extended cohort at pH 2.9.

In comparison, the compact and extended protein cohorts are not as evident for apo-MT1. Even at pH 7.4, we do not see a completely cooperative profile (Fig. 3J). This may indicate that some exposed cysteines are closer to the surface of apo-MT1 at physiological pH, which then bind the NEM in a noncooperative profile without disrupting the conformation and triggering the formation of NEM₂₀MT1. The clear switch from compact to extended conformations seen with MT3 is not present, indicating that apo-MT1 adopts a continuum of structures when it unfolds from the more compact structure at pH 7.4.

The cysteine modification reactions suggest that apo-MT1 adopts a more open conformation at pH 5 compared with MT3 at the same pH (Figs. 3ii and 2ii, respectively). The conformation of apo-MT1 resembles most closely that of apo-MT3 at pH 2.9, corresponding to an extended conformation. Based on the evidence that MT1 adopts a less compact structure with more exposed cysteines than MT3 at pH 7.4, it follows that this conformation would be more easily disrupted by acidic conditions.

To further corroborate this statement, we can refer to Figure 4, where the addition of up to 4 M GdmCl to apo-MT3 does not change the cysteine modification profile. We interpret this as the result of the continuing presence of the

compact protein with its inaccessible cysteines, where the modification reaction follows the cooperative pathway of Equation 1. This is highly unusual because in the presence of 4 M GdmCl, most proteins will denature, even those without formal structure such as MTs (47–52). The lack of evidence that the apo-MT3 has denatured despite apo-MT1 fully denaturing under the same conditions suggests that the GdmCl is not strong enough to disrupt the hydrogen bonds and van der Waals interactions that are the stabilizing forces of compact apo-MT3.

We can model the mixed reactions of apo-MTs described by Equations 1 and 2 using Tenua kinetic simulation software (Fig. 9). In these models, we assign the simulated rate constants ($k_{on(1-20)}$) as follows: 1, 100, 110, 120, 130, 140, 150, 160, 170, 180, 190, 200, 210, 220, 230, 240, 250, 260, 270, 12,000 (for cooperative modification, Fig. 9A) and 100, 63, 40, 25, 16, 10, 6.3, 4.0, 2.5, 1.6, 1.0, 0.63, 0.40, 0.25, 0.16, 0.1, 0.063, 0.040, 0.025, and 0.016 (for noncooperative modification, Fig. 9C). Figure 9E depicts the average of the two series of species in Figure 9, A and C, modeling the presence of two different compact states. For the cooperative Equation 1, the k_{20} has a greater value than k_{1-19} , with k_1 being the rate-limiting step as the protein is compact and cysteines are inaccessible. For the noncooperative Equation 2 pathway, k_{1-20} decreases as the number of NEM modifications increases, representing the statistical reduction of available sites. Figure 9, B, D, and F

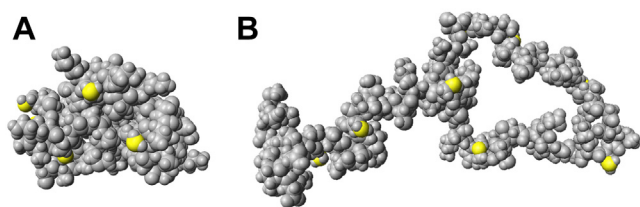


Figure 8. Calculated models of the open conformation (A) and closed conformation (B) of apo-MT1 using molecular mechanics and molecular dynamics methods. The yellow residues represent cysteines. (A) space-filling model of apo-MT1 calculated under 300 K conditions for 1000 ps with a 0.02-ps equilibration time. (B) space-filling model of apo-MT1 calculated under 1000 K conditions for 1000 ps with a 0.02-ps equilibration time.

show that the predicted mass spectra calculated using the modeled binding constants closely resemble the experimental mass spectra reported in Figure 2. This simulation clearly shows the presence of cooperative and a noncooperative modification mechanisms, representing a compact and extended conformation of apo-MT3, respectively. In contrast, the experimental data for apo-MT1 (Fig. 3) does not resemble the simulated data for either the completely cooperative or completely noncooperative models, indicating that we cannot model apo-MT1 as fully compact or fully extended.

Cysteine modification and metalation kinetics support the compact structure of apo-MT3

Further analysis of the modification rates of the cysteinyl thiols of MTs in the context of kinetics clarifies differences in cysteine accessibility. Apo-MT1 is modified faster than apo-MT3, which we can interpret as due to the greater cysteine accessibility in apo-MT1. It is clear from the NEM modification reactions and GdmCl denaturation studies described in Figures 2–4 that the apo-MT3 native structure is more robust than the structure of apo-MT1 (53). Therefore, we attribute the lower rate of modification in apo-MT3 to the presence of a more compact conformation, where cysteines are more deeply buried and thus inaccessible to the NEM molecules, as previously reported for other proteins (30).

Interestingly, the use of GdmCl as a denaturing agent did not increase the rate of modification or increase the accessibility of the cysteines (Fig. S1). For kinetic experiments, the bulky structures of GdmCl and NEM compared with the 8 kDa apo-MT protein may become particularly important. GdmCl disrupts salt bridges and interacts with charged residues and the protein backbone, thus blocking the sites of NEM modification and affecting its reaction kinetics (54–58).

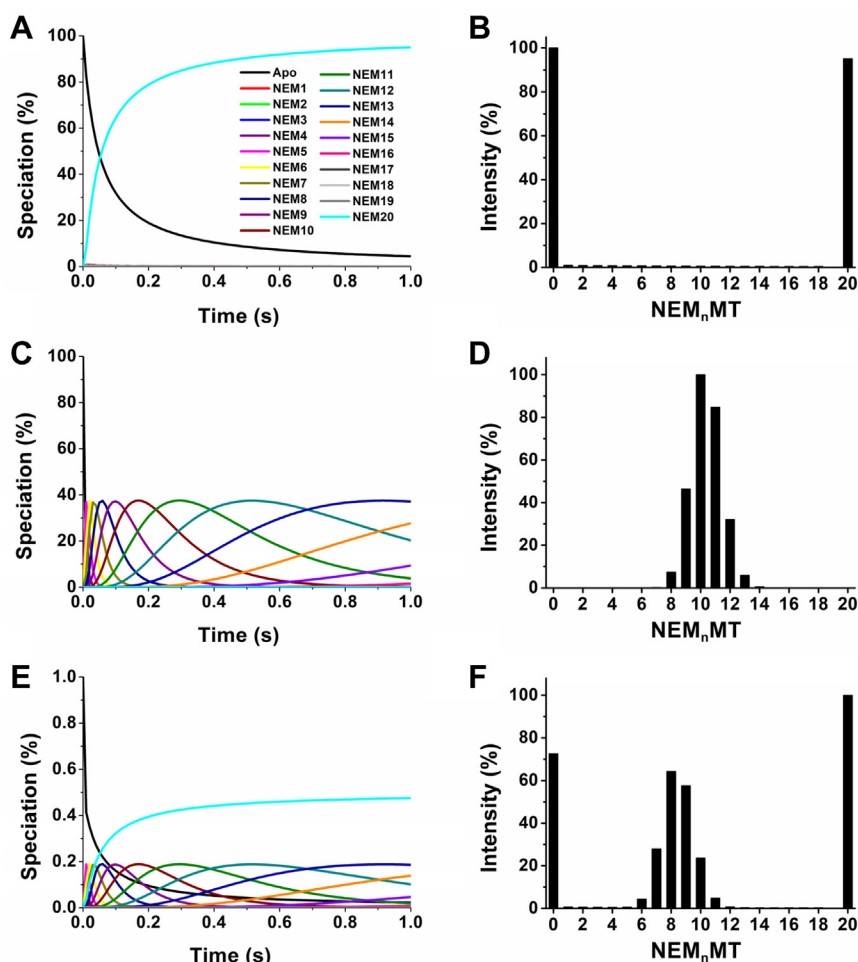


Figure 9. Simulated kinetics of N-ethylmaleimide modification of apo-MT. A, C, and E show the simulated speciation, and B, D, and F show the predicted mass spectra from a cross section at 0.05 s (B from A), 0.2 s (D from C), and 0.07 s (F from E). A and B represent apo-MT as completely compact, C and D represents apo-MT as completely extended, and E and F represent apo-MT as 50% compact and 50% extended.

Apo-metallothionein-3 cooperatively forms compact structures

The Cd^{2+} metalation kinetics of apo-MT3 compared with apo-MT1 shows the opposite pattern, where apo-MT3 metalates faster than apo-MT1 (Fig. 5ii). Since the seven Cd^{2+} are coordinated into two domains each involving terminal and bridging cysteines, our interpretation is that the more compact structure of the apo-MT3 has cysteines that are closer together and, thus, metalates faster. When GdmCl was added to the solutions, the metalation reactions of the apo-MTs were slower, reflecting the expansion of the protein. Although GdmCl does slow the metalation rate of apo-MT3, the fitted rate constant is not significantly different to that of apo-MT1 in the absence of GdmCl. We suggest that, in the presence of 4 M GdmCl, apo-MT3 has adopted a structure similar to native apo-MT1, where the protein is still compact but not as tightly compressed as its native state. We suggest that this effect is not a result of GdmCl blocking sites as seen with NEM because a melting curve of denaturation has been determined in the past with MTs (59, 60).

IM-MS provides direct evidence of compact and extended conformations of apo-MT3

To this point, only indirect data were used to support the compact conformation of apo-MT3. Using IM-MS, we determined two CCS values for two conformational populations of apo-MT3, which shift according to pH for the 7+ charge state (Fig. 6). Interestingly, we do not see these populations in other charge states. We speculate that this is because lower charge states such as 5+ may only encompass the compact conformation, whereas higher charge states such as 10+ are only seen for the expanded conformation. In contrast, both the compact and extended conformations adopt a 7+ charge in the mass spectrometer under the conditions listed. For IM-MS, the conditions used such as wave height, wave velocity, and IMS gas pressure greatly affect the drift times and protein populations, even for homogenous metalated species of MT (36, 42, 61). Therefore, it is important to compare within each charge state under the same IM-MS parameters for conclusions to be made about the protein.

The data provided by the IM-MS method show the decreasing presence of the compact and ordered conformation and the increase of the expanded conformation clearly in Figure 6E. This provides direct evidence of the two distinct states that exist for apo-MT3, corroborated by the cysteine modification profiles measured using the ESI-MS. Further analysis of this finding can be accomplished using molecular modeling.

Molecular modeling illustrates the conformations and modification changes of apo-MT3

To further provide support for our proposed structure, molecular modeling was undertaken. Figure 7I shows proposed models of the expanded and compact structures, with the 1000 K condition model representing the extended conformation and the 300 K condition model representing the compact conformation of apo-MT3. The NEM modification of the modeled apo-MT3 (Fig. 7ii) illustrates the cooperative

effect of the stepwise modification seen in Figure 2I—modified cysteines trigger the exposure of subsequent cysteines until the full protein is modified as a result of the changing of MT3 structure upon NEM binding. With respect to the surface accessibility, in comparison with apo-MT3, we see that the surface accessibility is lower for the expanded structure of apo-MT1 and higher for the compact structure of apo-MT1 (Fig. 8). The surface accessibility is smaller for the expanded structure of apo-MT1 compared with apo-MT3 because of the shorter polypeptide chain of apo-MT1, which does not have the acidic loop insert in the α domain.

Taken together, our data suggest that the structure of apo-MT3 under physiological conditions forms a compact structure with buried cysteines. In contrast, extended IDPs show a continuum of conformations where an unfolded conformation will gradually turn into a more compact conformation (62). The data described here shows a two-state conformation change mechanism that is commonly seen with folded and ordered proteins (63, 64). Therefore, although apo-MT3 is not formally folded, we propose that apo-MT3 has an ordered and compact structure under physiological conditions and is not a traditional IDP.

Physiological implications of apo-MT3 as an unusually compact structure

Apo-MT3 exists in structured and compact conformations rather than as a traditional IDP according to combined results from our study. This property is consistent with molten globule behavior, where there are no formal secondary structures such as an alpha helix or beta sheet and also no continuum of unfolding (62). This two-step folding property with no specific intermediates is common for small folded proteins, and although there is no evidence for a folding in the traditional sense, apo-MT3 shares many properties with those of a folded protein (65, 66).

In contrast, the well-known structures of metalated MTs comprising the two metal-binding domains are completely dependent on the metal to protein stoichiometry and only present when bound to exactly seven Zn^{2+} or Cd^{2+} ions (6, 67). With either fewer than seven or more than seven, different structures are expected. With one to five Zn^{2+} or Cd^{2+} at physiological pH, structures where the metals are terminally bound are dominant and not the traditional cluster structures (68–70). Above seven, a supermetalated cluster has been reported for Cd^{2+} in MT1 (71). These structures are also pH dependent so that the beaded, or terminally coordinated, structure will coalesce to a cluster structure at lower pH (35). For MT3 specifically, a partial structure of $\text{Cd}_7\text{MT3}$ was determined by Wang *et al.* using ^{113}Cd , ^{113}Cd - ^1H HSQC, and ^{15}N - ^1H NMR spectroscopy (18). The structure of the metalated β domain was determined to be comparatively fluxional according to two independent NMR studies (18, 72).

Previous studies on the metalated forms of MT3 allows for the interpretation of the significance of the compact apo-MT3 conformation. In particular, its biological function as a signaling protein may be impacted. In order to induce its

growth inhibitory activity and other effects, MT3 participates in a series of protein–protein interactions (15, 73–75). Because the apo-MT3 structure remains unusually compact even in the absence of metals, these biochemical pathways may be activated with apo-MT3 as well as partially metalated MT3. Specifically, the essential amino acids for growth inhibitory activity, the unique Thr5 and Glu23 residues, and the motif TCPCP in the β domain may be exposed in this highly compact conformation, allowing for the essential protein–protein interactions to take place (72, 76–78). Our report that the apo-MT3 structure is a highly compact and stable protein may allow for protein–protein interactions and subsequent functions such as its growth inhibitory activity even when it is not fully metalated.

It is important to consider how the reduced cysteines are maintained in the brain-located apo-MT3 as a 20-cysteine apoprotein after it is newly synthesized. For the metal-induced MT1 and MT2, the free metal ion density would be high in the region of the newly synthesized apoprotein, thus protecting the reactive thiols of the 20 cysteines. However, in contrast, MT3 is not metal induced but constitutively expressed and induced by oxidative processes; therefore, it must survive in an apo form for more extended periods than MT1 and MT2 (79–81). The compact nature of apo-MT3 that we describe here also allows the rate of metalation to be extremely high, providing rapid protection of its cysteines when metal ions are available.

This report on apo-MT3 is important due to apo-MT3's multiple roles in physiological health. In relation to its role in neuronal growth and its link to neurodegenerative diseases, it has been proposed that, by regulating actin polymerization and the cytoskeleton structure, a decrease in uptake of amyloid beta plaques occurs, a key marker of Alzheimer's disease (15). This may be a possible mechanism for neurodegeneration and the presence of plaques forming extracellularly (24). Zn-MT3, therefore, has been administered to increase solubilization of amyloid beta plaques in a mouse model (17). MT3 also regulates lysosomes and endosomes through cytoskeleton interactions, crucial components of the process of autophagy, and recycling of materials in diseased cells and normal cells (27). MT3 was found as a distinct marker in different forms of cancer of the adrenal glands, hepatocellular carcinoma, and triple-negative breast cancer (81–84). MT3 plays an important role in neuroblastoma and in the processes underlying light exposure of the retina, where an MT3 knockout model was shown to induce retinal degeneration (85, 86).

Considering the multiple physiological functions, interactions, and the possible treatment potential of MT3, understanding the *de novo* structure of apo-MT3 is one step closer to unveiling its structure–function relationships.

In conclusion, we report from ESI-MS and cysteine modification studies, stopped flow kinetics of cysteine modification and metalation studies, IM-MS, and molecular dynamics calculations that apo-MT3 cooperatively adopts a compact and stable structure under physiological conditions. The data support a model in which apo-MT3 exists as either an extraordinarily compact or completely expanded conformer

rather than a continuum of expanded structures expected with intrinsically disordered proteins. This property allows for the enhanced physiological stability of apo-MT3, differential binding kinetics to metals, and isoform-specific protein–protein interactions.

Experimental procedures

MT3 expression

Recombinant human metallothionein 3 was cloned into pET29a plasmids using restriction enzymes NcoI and HindIII completed by GENEWIZ. The plasmid vectors were transformed into BL21 (DE3) competent *Escherichia coli* cells using procedures outlined by GENEWIZ. A glycerol stock of the transformed cells containing 9:1 (v/v) cell culture/80% glycerol was prepared. The MT3 sequence is as follows: GSMGK AAAA MDPETCPCPSGGGCT CADSCKCEGC KCTSCCK SCC SCCPAECEKC AKDCVCKGGE AAEEAEKCS CCQKK AAAA. The mass of apo-MT3 is 8210 Da and that of Cd₇MT3 is 8985 Da.

MT3 purification

Cells from the glycerol stock stored at -80°C were grown in miniprep quantities in LB broth (BioShop) with 50 mg mL^{-1} kanamycin sulphate (AG Scientific) and incubated at 37°C overnight. Cell colonies were then transferred to $4 \times 1\text{ L}$ LB broth cultures containing 1 ml of 50 mg mL^{-1} kanamycin sulfate solution and $50\text{ }\mu\text{l}$ of 1 M CdSO₄ solution. Cultures were left for approximately 3 h until an absorbance of 0.4 to 0.6 was reached at 600 nm. Isopropyl- β -D-thiogalactoside (IPTG, BioShop) was added to a final concentration of 0.4 mM to induce protein expression followed by $400\text{ }\mu\text{l}$ of 1 M CdSO₄ solution and grown for an additional 3 h. Cells were pelleted through centrifugation (Avanti J-26 XPI fixed rotor centrifuge, Beckman Coulter, Toronto, Canada) and suspended in deaerated tris-hydroxymethyl-aminomethane HCl (Tris-HCl) buffer (Sigma Aldrich) at pH 7.4 and stored at -80°C . Cells were lysed in pH 7.4 Tris-HCl buffer using a cell homogenizer (Constant Systems) at 18 to 22 kPa. The cell lysate was subjected to centrifugation at 13,000 rpm for 40 min. The pH of the supernatant was lowered to pH 2 with concentrated HCl in order to precipitate most proteins excluding MT3. This mixture was again centrifuged for 15 min at 13,000 rpm. The supernatant was collected and pH adjusted to pH 7.4 using ammonium hydroxide (Honeywell). The solution was then loaded onto a DEAE anion exchange column, where the flow-through containing the MT3 protein was collected. The MT3 was concentrated to 20 ml using a stirred ultrafiltration cell (EMD Millipore) with a 5 kDa cellulose membrane under nitrogen gas pressure. The S-tag was then removed with a Thrombin CleanCleave kit (Sigma Aldrich) following the manufacturer's instructions. The MT3 solution containing the liberated S-tag was then loaded onto a HiTrap SP Sepharose cation exchange column (GE Healthcare) with a capacity of 10 ml. The Cd-bound MT was isolated using an elution gradient of 10 mM Tris-HCl with an increasing amount of 1 M NaCl at pH 7 *via* HPLC (Dionex UltiMate 3000) using a

Apo-metallothionein-3 cooperatively forms compact structures

UV-visible absorption spectrophotometer (Cary 50, Agilent Technologies) to identify the eluent with the characteristic absorption at 250 nm (S–Cd ligand-to-metal charge transfer band). Aliquots of 1 ml of concentrated MT3 were stored at -80°C .

MT1 purification

The MT1 was cloned, transformed, and expressed in the same manner as with MT3. The sequence is as follows: GSMGKAAAAM DPNCSCATGG SCTCTGSKC KECK TSCCK SCCSCPMSC AKCAQGCICK GASEKSCCA KKAAAA. The mass of apo-MT1 is 7406 Da, and the mass of $\text{Cd}_7\text{MT1}$ is 8179 Da.

The cells containing the expressed MT1 were lysed in the same manner as with MT3. The lysate was centrifuged at 13,000 rpm for 40 min. The supernatant was collected and loaded onto a HighTrap SP Sepharose cation exchange column and washed with 10 mM Tris-HCl at pH 7.4. The MT1 was isolated by applying a salt gradient (10 mM Tris-HCl containing increasing amounts of 1 M NaCl at pH 7.4) using HPLC. The process was monitored through the S–Cd Ligand to Metal Charge Transfer at 250 nm using a UV-visible absorption spectrometer.

The MT1 was then concentrated and the S-tag was cleaved using the same procedure as used for MT3. To purify the MT1 from the S-tag, the cation exchange procedure was repeated and the protein solution was concentrated to approximately 20 ml. Aliquots of 1 ml were stored at -80°C .

Apo-MT preparation

All solutions of MT and buffers are evacuated then back-filled with argon gas in a custom-designed vacuum chamber to ensure an anaerobic environment. This procedure refers to the preparation of MT1 and MT3. MT was demetalated using pH 2 ammonium formate with 1 mM tris(2-carboxyethyl) phosphine (TCEP)-HCl (Soltec Ventures) loaded onto PD-10 desalting columns (GE Healthcare) and isolated as per manufacturer's instructions. It was then transferred to an Amicon Ultra-4 centrifugal filter tube (5 kDa MWCO, Millipore) and centrifuged at 4000 rpm with a swing-bucket rotor for 10 min. MT was subsequently desalted using pH 7.4 ammonium formate with 1 mM TCEP loaded onto the PD-10 desalting columns before buffer exchange with Amicon Ultra-4 centrifugal filter tube to pH 7.4.

Concentrations of MT were determined using $\epsilon_{250\text{nm}} = 89,000 \text{ M}^{-1} \text{ cm}^{-1}$ when in solution with excess Cd^{2+} .

Solution preparation

Guanidinium chloride (GdmCl) was made using GdmCl crystals (Sigma Aldrich) dissolved in 20 mM ammonium formate buffer. The mixture was gently heated and stirred until all crystals had dissolved. The pH was adjusted after cooling to pH 7.4 and the concentration was adjusted to 8 M.

Ten millimolar solutions of NEM (Thermo Scientific) and $\text{Cd}(\text{OAc})_2$ (Acros) were prepared in deionized water.

GdmCl and NEM modification reactions were conducted according to previously published protocols (50). Briefly, apo-MT3 was mixed with appropriate volumes of a stock solution of 8 M GdmCl solution to make final concentrations of 1 to 4 M GdmCl. This mixture was left to equilibrate for at least 30 min. Ten molar equivalents of the NEM cysteine modifier was then added and left to equilibrate for at least 30 min before buffer exchange with 20 mM ammonium formate, pH 7.4, using PD10 desalting columns. The sample was then concentrated before introduction into the ESI-MS.

ESI-MS procedures

The pH of each solution was adjusted according to the required pH values using 20 mM ammonium formate buffer exchange, dilute deaerated ammonium hydroxide, and/or dilute deaerated formic acid. ESI mass spectral data were collected using a Bruker Micro-TOF II spectrometer (Bruker Daltonics), calibrated with NaI in the positive ion mode. Settings: scan = 1000 to 4000 m/z ; rolling average = 2; nebulizer = 2 bar; dry gas = 130°C @ 8.0 L min^{-1} ; capillary = 4000 V; end plate offset = -500 V ; capillary exit = 175 V; skimmer 1 = 30.0 V; skimmer 2 = 23.5 V; hexapole RF = 800 V. Spectra were collected for 1 to 3 min and deconvoluted with the maximum entropy application of the Bruker Compass Data Analysis software.

IMS procedures

The pH of the protein samples was adjusted in the same manner as for the samples used for the ESI-MS measurements. Ion mobility mass spectra were collected with a Waters Synapt HDMS G1 time-of-flight mass spectrometer (Waters). The standard Z-spray source was used with a desolvation gas flow rate of 500 L h^{-1} . Samples were infused at $5 \mu\text{l min}^{-1}$. NaI was used to calibrate the instrument in positive ion mode, with settings of +1.5 kV capillary voltage, 15 V sampling cone voltage, and 3 V extraction cone voltage. For protein samples, a capillary voltage of +1.4 kV was used, with 10 V sample cone voltage and 1 V extraction cone voltage. The backing pressure was set to 5 mbar by a SpeediValve on the scroll pump. The cone gas flow rate was 50 L h^{-1} . The source temperature was 25°C , and the desolvation temperature was 40°C . The trap collision energy was set to 2 V, whereas the transfer collision energy was set to 4 V. The trap DC entrance was 1 V, the trap bias was set to 9 V, and the trap exit was set to 5 V. The trap wave velocity was set to 100 m s^{-1} with a wave height of 0.1 V. The IMS entrance was set to 6.7 V, and IMS exit was 0 V, with a wave velocity to 300 m s^{-1} with a wave height of 6.5 V. The transfer entrance was set to 1 V, the transfer exit was set to 0 V, and transfer wave velocity was set to 247 m s^{-1} with a wave height of 4 V. The trap release time was 500 μs , and its trap height was 8 V with an extract height of 0 V. The transfer trap height was set to 12 V and the extract height to 8 V. The IMS gas was set to 6 ml min^{-1} .

Stopped flow procedures

Apo-MT was prepared as stated above and diluted to a concentration of 2.5 μM for cadmium metalation experiments and 10 μM for NEM modification experiments. Solutions of

Cd(OAc)₂ were 17.5 μM, which is equal to 7 mol. eq. Solutions of NEM were 400 μM. An SFM-400 stopped-flow apparatus (BioLogic) and a MOS-250 UV-visible absorption spectrophotometer was used with a 10-mm path length and 1-mm aperture quartz cuvette for both metalation and modification experiments.

For NEM modification experiments, 160 μl of the NEM solution and 160 μl of the protein solution were transferred into the cuvette at a total rate of 8 ml s⁻¹ for 80 ms. The reaction was mixed and, following a deadtime of 4 ms, was monitored every 1 ms for 8 s at 300 nm. The process was repeated at least 3 times and the data were averaged.

For the cadmium metalation experiments, 120 μl of the cadmium solution and 120 μl of the protein solution were transferred into the cuvette at a rate of 8 ml s⁻¹ for 60 ms. The reaction was mixed and, following a deadtime of 4 ms, was monitored every 500 μs for 4 s at 250 nm. The process was repeated at least 3 times and the data were averaged. For GdmCl experiments, deionized water was used to flush the cuvette before every measurement.

Fitting of kinetic traces

The NEM data were transformed from absorbance to concentration units using Beer's law and $\epsilon_{300\text{nm}} = 620 \text{ M}^{-1} \text{ cm}^{-1}$. The weak interaction between TCEP and the NEM was accounted for by carrying out kinetic experiments between NEM and 1 mM TCEP and subtracting the resultant change in absorbance from the data recorded for the protein. The Cd(OAc)₂ metalation data was transformed to concentration units using Beer's law and $\epsilon_{250\text{nm}} = 89,000 \text{ M}^{-1} \text{ cm}^{-1}$ for non-GdmCl solutions. For GdmCl solutions, owing to the increased absorption of the charge transfer band at 250 nm, the concentration was back-calculated using known values of expected concentration from the Cd(OAc)₂ metalation experiments in the absence of GdmCl.

Copasi version 4.30 was used to fit kinetic traces with rate constants (87). The data were fit as a single bimolecular reaction for both modification and metalation reactions. The standard deviations of all replicates given by Copasi were used to determine a standard error for the final report of the rate constant. The statistical tests were completed using the two-sample *t* test function of Origin 8.5.

Molecular modeling

Molecular models were calculated using Scigress Version 6.0.0 (Fujitsu Poland Ltd). Models were first calculated using molecular mechanics calculations (MM3); then, molecular dynamics calculations were carried out at 300 and 1000 K for 1000 ps, with an equilibrium of 0.02 ps and a dielectric constant for water of 78.5.

Tenua procedures

Tenua 2.1, a chemical kinetics simulation program, based on KINSIM by Barshop, Wrenn, and Frieden, was used to simulate the titration using decreasing rate constants for the

noncooperative simulation and higher binding constants for the dominant species for the cooperative simulation (88).

Data availability

All data supporting the statements made are included in this article and in Supplementary Information.

Supporting information—This article contains supporting information.

Acknowledgments—We would like to thank John Vanstone and the members of the University of Western Ontario Electronics Shop for the maintenance of our instruments. We thank Dr Haidy Metwally for assistance with the ESI-MS and ion mobility MS.

Author contributions—A. T. Y., N. C. K., M. J. S. conceptualization; A. T. Y., N. C. K., M. J. S. formal analysis; A. T. Y., N. C. K. investigation; A. T. Y. writing – original draft; A. T. Y., N. C. K., M. J. S. writing – review & editing.

Funding and additional information—We would like to thank NSERC for Discovery Grant number 06545-2020 (to M. J. S.), NSERC for CGS-D (to A. T. Y.), and NSERC for PGS-D (to N. C. K.).

Conflicts of interest—The authors declare that they have no conflicts of interest with the contents of this article.

Abbreviations—The abbreviations used are: CCS, collision cross section; ESI-MS, electrospray ionization mass spectroscopy; GdmCl, guanidinium chloride; IDP, intrinsically disordered protein; IM-MS, ion mobility mass spectrometry; MT, metallothionein; NEM, N-ethylmaleimide.

References

- Lu, Y., Yeung, N., Sieracki, N., and Marshall, N. M. (2009) Design of functional metalloproteins. *Nature* **460**, 855–862
- Waldron, K. J., Rutherford, J. C., Ford, D., and Robinson, N. J. (2009) Metalloproteins and metal sensing. *Nature* **460**, 823–830
- Zhang, Y., and Zheng, J. (2020) Bioinformatics of metalloproteins and metalloproteomes. *Molecules* **25**, 3366
- Supuran, C. T. (2016) Structure and function of carbonic anhydrases. *Biochem. J.* **473**, 2023–2032
- Palmiter, R. D. (1998) The elusive function of metallothioneins. *Proc. Natl. Acad. Sci. U. S. A.* **95**, 8428–8430
- Sutherland, D. E. K., and Stillman, M. J. (2011) The “magic numbers” of metallothionein. *Metallomics* **3**, 444–463
- Wong, D. L., and Stillman, M. J. (2018) Capturing platinum in cisplatin: kinetic reactions with recombinant human apo-metallothionein 1a. *Metallomics* **10**, 713–721
- Robbins, A. H., McRee, D. E., Williamson, M., Collett, S. A., Xuong, N. H., Furey, W. F., *et al.* (1991) Refined crystal structure of Cd, Zn metallothionein at 2.0 Å resolution. *J. Mol. Biol.* **221**, 1269–1293
- Braun, W., Vasák, M., Robbins, A. H., Stout, C. D., Wagner, G., Kägi, J. H., *et al.* (1992) Comparison of the NMR solution structure and the x-ray crystal structure of rat metallothionein-2. *Proc. Natl. Acad. Sci. U. S. A.* **89**, 10124–10128
- Boulanger, Y., Armitage, I. M., Miklossy, K. A., and Winge, D. R. (1982) ¹¹³Cd NMR study of a metallothionein fragment. Evidence for a two-domain structure. *J. Biol. Chem.* **257**, 13717–13719
- Thirumoorthy, N., Shyam Sunder, A., Manisenthil Kumar, K. T., Senthil kumar, M., Ganesh, G. N. K., and Chatterjee, M. (2011) A review of

Apo-metallothionein-3 cooperatively forms compact structures

- metallothionein isoforms and their role in pathophysiology. *World J. Surg. Oncol.* **9**, 54
- Vašák, M., and Meloni, G. (2017) Mammalian metallothionein-3: new functional and structural insights. *Int. J. Mol. Sci.* **18**, 1117
 - Hozumi, I., Suzuki, J. S., Kanazawa, H., Hara, A., Saio, M., Inuzuka, T., et al. (2008) Metallothionein-3 is expressed in the brain and various peripheral organs of the rat. *Neurosci. Lett.* **438**, 54–58
 - Jiang, Z., Shen, B., and Xiang, J. (2019) Metal-dependent interactions of metallothionein-3 β -domain with amyloid- β peptide and related physiological implications. *J. Inorg. Biochem.* **196**, 110693
 - Koh, J. Y., and Lee, S. J. (2020) Metallothionein-3 as a multifunctional player in the control of cellular processes and diseases. *Mol. Brain* **13**, 116
 - Uchida, Y., Takio, K., Titani, K., Ihara, Y., and Tomonaga, M. (1991) The growth inhibitory factor that is deficient in the Alzheimer's disease brain is a 68 amino acid metallothionein-like protein. *Neuron* **7**, 337–347
 - Manso, Y., Carrasco, J., Comes, G., Meloni, G., Adlard, P. A., Bush, A. I., et al. (2012) Characterization of the role of metallothionein-3 in an animal model of Alzheimer's disease. *Cell. Mol. Life Sci.* **69**, 3683–3700
 - Wang, H., Zhang, Q., Cai, B., Li, H., Sze, K.-H., Huang, Z.-X., et al. (2006) Solution structure and dynamics of human metallothionein-3 (MT-3). *FEBS Lett.* **580**, 795–800
 - Yang, Y., Maret, W., and Vallee, B. L. (2001) Differential fluorescence labeling of cysteinyl clusters uncovers high tissue levels of thionein. *Proc. Natl. Acad. Sci. U. S. A.* **98**, 5556–5559
 - Petering, D. H., Zhu, J., Krezoski, S., Meeusen, J., Kiekenbush, C., Krull, S., et al. (2006) Apo-metallothionein emerging as a major player in the cellular activities of metallothionein. *Exp. Biol. Med.* **231**, 1528–1534
 - Rigby, K. E., Chan, J., Mackie, J., and Stillman, M. J. (2006) Molecular dynamics study on the folding and metallation of the individual domains of metallothionein. *Proteins: Struct. Funct. Bioinform.* **62**, 159–172
 - Scheller, J. S., Irvine, G. W., Wong, D. L., Hartwig, A., and Stillman, M. J. (2017) Stepwise copper(i) binding to metallothionein: a mixed cooperative and non-cooperative mechanism for all 20 copper ions. *Metallomics* **9**, 447–462
 - Summers, K. L., Mahrok, A. K., Dryden, M. D. M., and Stillman, M. J. (2012) Structural properties of metal-free apometallothioneins. *Biochem. Biophys. Res. Commun.* **425**, 485–492
 - Lee, S.-J., Seo, B.-R., and Koh, J.-Y. (2015) Metallothionein-3 modulates the amyloid β endocytosis of astrocytes through its effects on actin polymerization. *Mol. Brain* **8**, 84
 - Lee, S.-J., and Koh, J.-Y. (2010) Roles of zinc and metallothionein-3 in oxidative stress-induced lysosomal dysfunction, cell death, and autophagy in neurons and astrocytes. *Mol. Brain* **3**, 30
 - Moffatt, P., and SÉGuin, C. (1998) Expression of the gene encoding metallothionein-3 in organs of the reproductive system. *DNA Cell Biol.* **17**, 501–510
 - Cho, Y. H., Lee, S.-H., Lee, S.-J., Kim, H. N., and Koh, J.-Y. (2020) A role of metallothionein-3 in radiation-induced autophagy in glioma cells. *Sci. Rep.* **10**, 2015
 - Chowdhury, D., Alrefai, H., Landero Figueroa, J. A., Candor, K., Porollo, A., Fecher, R., et al. (2019) Metallothionein 3 controls the phenotype and metabolic programming of alternatively activated macrophages. *Cell Rep.* **27**, 3873–3886.e3877
 - Wong, D. L., Korkola, N. C., and Stillman, M. J. (2019) Kinetics of competitive Cd²⁺ binding pathways: the realistic structure of intrinsically disordered, partially metallated metallothioneins. *Metallomics* **11**, 894–905
 - Britto, P. J., Knipling, L., McPhie, P., and Wolff, J. (2005) Thiol-disulphide interchange in tubulin: kinetics and the effect on polymerization. *Biochem. J.* **389**, 549–558
 - Winther, J. R., and Thorpe, C. (2014) Quantification of thiols and disulfides. *Biochim. Biophys. Acta* **1840**, 838–846
 - Alexander, N. M. (1958) Spectrophotometric assay for sulfhydryl groups using N-ethylmaleimide. *Anal. Chem.* **30**, 1292–1294
 - Gorin, G., Martic, P. A., and Doughty, G. (1966) Kinetics of the reaction of N-ethylmaleimide with cysteine and some congeners. *Arch. Biochem. Biophys.* **115**, 593–597
 - Roberts, E., and Rouser, G. (1958) Spectrophotometric assay for reaction of N-ethylmaleimide with sulfhydryl groups. *Anal. Chem.* **30**, 1291–1292
 - Irvine, G. W., Pinter, T. B., and Stillman, M. J. (2016) Defining the metal binding pathways of human metallothionein 1a: balancing zinc availability and cadmium seclusion. *Metallomics* **8**, 71–81
 - Sun, Y., Vahidi, S., Sowole, M. A., and Konermann, L. (2016) Protein structural studies by traveling wave ion mobility spectrometry: a critical look at electrospray sources and calibration issues. *J. Am. Soc. Mass Spectrom.* **27**, 31–40
 - Ben-Nissan, G., and Sharon, M. (2018) The application of ion-mobility mass spectrometry for structure/function investigation of protein complexes. *Curr. Opin. Chem. Biol.* **42**, 25–33
 - Konijnenberg, A., Butterer, A., and Sobott, F. (2013) Native ion mobility-mass spectrometry and related methods in structural biology. *Biochim. Biophys. Acta* **1834**, 1239–1256
 - Giles, K., Pringle, S. D., Worthington, K. R., Little, D., Wildgoose, J. L., and Bateman, R. H. (2004) Applications of a travelling wave-based radio-frequency-only stacked ring ion guide. *Rapid Commun. Mass Spectrom.* **18**, 2401–2414
 - Hopper, J. T. S., and Oldham, N. J. (2009) Collision induced unfolding of protein ions in the gas phase studied by ion mobility-mass spectrometry: the effect of ligand binding on conformational stability. *J. Am. Soc. Mass Spectrom.* **20**, 1851–1858
 - Ruotolo, B. T., Benesch, J. L. P., Sandercock, A. M., Hyung, S.-J., and Robinson, C. V. (2008) Ion mobility-mass spectrometry analysis of large protein complexes. *Nat. Protoc.* **3**, 1139–1152
 - Chen, S.-H., and Russell, D. H. (2015) How closely related are conformations of protein ions sampled by IM-MS to native solution structures? *J. Am. Soc. Mass Spectrom.* **26**, 1433–1443
 - Chatterjee, T., Pal, A., Dey, S., Chatterjee, B. K., and Chakrabarti, P. (2012) Interaction of virstatin with human serum albumin: spectroscopic analysis and molecular modeling. *PLoS One* **7**, e37468
 - Fraczkiewicz, R., and Braun, W. (1998) Exact and efficient analytical calculation of the accessible surface areas and their gradients for macromolecules. *J. Comput. Chem.* **19**, 319–333
 - Gumerov, D. R., Dobo, A., and Kaltashov, I. A. (2002) Protein-ion charge-state distributions in electrospray ionization mass spectrometry: distinguishing conformational contributions from masking effects. *Eur. J. Mass Spectrom.* **8**, 123–129
 - Dobo, A., and Kaltashov, I. A. (2001) Detection of multiple protein conformational ensembles in solution via deconvolution of charge-state distributions in ESI MS. *Anal. Chem.* **73**, 4763–4773
 - Singh, R., Hassan, M. I., Islam, A., and Ahmad, F. (2015) Cooperative unfolding of residual structure in heat denatured proteins by urea and guanidinium chloride. *PLoS One* **10**, e0128740
 - Gupta, P., Khan, F. I., Ambreen, D., Lai, D., Alajmi, M. F., Hussain, A., et al. (2020) Investigation of guanidinium chloride-induced unfolding pathway of sphingosine kinase 1. *Int. J. Biol. Macromol.* **147**, 177–186
 - Khan, S. H., Prakash, A., Pandey, P., Lynn, A. M., Islam, A., Hassan, M. I., et al. (2019) Protein folding: molecular dynamics simulations and *in vitro* studies for probing mechanism of urea- and guanidinium chloride-induced unfolding of horse cytochrome-c. *Int. J. Biol. Macromol.* **122**, 695–704
 - Irvine, G. W., Korkola, N., and Stillman, M. J. (2018) Isolated domains of recombinant human apo-metallothionein 1A are folded at neutral pH: a denaturant and heat-induced unfolding study using ESI-MS. *Biosci. Rep.* **38**, BSR20180592
 - Andersen, K. K., Wang, H., and Otzen, D. E. (2012) A kinetic analysis of the folding and unfolding of OmpA in urea and guanidinium chloride: single and parallel pathways. *Biochemistry* **51**, 8371–8383
 - Akhtar, M. S., Ahmad, A., and Bhakuni, V. (2002) Guanidinium chloride- and urea-induced unfolding of the dimeric enzyme glucose oxidase. *Biochemistry* **41**, 3819–3827
 - Irvine, G. W., Santolini, M., and Stillman, M. J. (2017) Selective cysteine modification of metal-free human metallothionein 1a and its isolated domain fragments: solution structural properties revealed via ESI-MS. *Protein Sci.* **26**, 960–971

54. Mandal, M., and Mukhopadhyay, C. (2014) Microsecond molecular dynamics simulation of guanidinium chloride induced unfolding of ubiquitin. *Phys. Chem. Chem. Phys.* **16**, 21706–21716
55. Meuzelaar, H., Panman, M. R., and Woutersen, S. (2015) Guanidinium-induced denaturation by breaking of salt bridges. *Angew. Chem. Int. Ed.* **54**, 15255–15259
56. Ganguly, P., and Shea, J.-E. (2019) Distinct and nonadditive effects of urea and guanidinium chloride on peptide solvation. *J. Phys. Chem. Lett.* **10**, 7406–7413
57. O'Brien, E. P., Dima, R. I., Brooks, B., and Thirumalai, D. (2007) Interactions between hydrophobic and ionic solutes in aqueous guanidinium chloride and urea solutions: lessons for protein denaturation mechanism. *J. Am. Chem. Soc.* **129**, 7346–7353
58. Macdonald, R. D., and Khajepour, M. (2015) Effects of the protein denaturant guanidinium chloride on aqueous hydrophobic contact-pair interactions. *Biophys. Chem.* **196**, 25–32
59. Irvine, G. W., Duncan, K. E., Gullons, M., and Stillman, M. J. (2015) Metalation kinetics of the human α -metallothionein 1a fragment is dependent on the fluxional structure of the apo-protein. *Chem. Eur. J.* **21**, 1269–1279
60. Kumar, A., and Pawar, S. S. (2002) The aqueous salt-promoted Diels–Alder reaction of anthracene-9-carbinol with N-ethylmaleimide. *Tetrahedron* **58**, 1745–1749
61. Atmanene, C., Petiot-Bécard, S., Zeyer, D., Van Dorsselaer, A., Vivat Hannah, V., and Sanglier-Cianféron, S. (2012) Exploring key parameters to detect subtle ligand-induced protein conformational changes using traveling wave ion mobility mass spectrometry. *Anal. Chem.* **84**, 4703–4710
62. Uversky, V. N. (2009) Intrinsically disordered proteins and their environment: Effects of strong denaturants, temperature, pH, counter ions, membranes, binding partners, osmolytes, and macromolecular crowding. *Protein J.* **28**, 305–325
63. Dunker, A. K., Lawson, J. D., Brown, C. J., Williams, R. M., Romero, P., Oh, J. S., et al. (2001) Intrinsically disordered protein. *J. Mol. Graph. Model.* **19**, 26–59
64. Finkelstein, A. V. (2018) 50+ years of protein folding. *Biochemistry (Moscow)* **83**, S3–S18
65. Jackson, S. E. (1998) How do small single-domain proteins fold? *Fold Des* **3**, R81–91
66. Huang, J.-T., and Cheng, J.-P. (2008) Differentiation between two-state and multi-state folding proteins based on sequence. *Proteins: Struct. Funct. Bioinform.* **72**, 44–49
67. Rigby Duncan, K. E., and Stillman, M. J. (2006) Metal-dependent protein folding: metallation of metallothionein. *J. Inorg. Biochem.* **100**, 2101–2107
68. Sutherland, D. E. K., Summers, K. L., and Stillman, M. J. (2012) Noncooperative metalation of metallothionein 1a and its isolated domains with zinc. *Biochemistry* **51**, 6690–6700
69. Palumaa, P., Eriste, E., Njankova, O., Pokras, L., Jörnvall, H., and Sillard, R. (2002) Brain-specific metallothionein-3 has higher metal-binding capacity than ubiquitous metallothioneins and binds metals non-cooperatively. *Biochemistry* **41**, 6158–6163
70. Jayawardena, D. P., Heinemann, I. U., and Stillman, M. J. (2017) Zinc binds non-cooperatively to human liver metallothionein 2a at physiological pH. *Biochem. Biophys. Res. Commun.* **493**, 650–653
71. Sutherland, D. E., Willans, M. J., and Stillman, M. J. (2012) Single domain metallothioneins: supermetalation of human MT 1a. *J. Am. Chem. Soc.* **134**, 3290–3299
72. Hasler, D. W., Jensen, L. T., Zerbe, O., Winge, D. R., and Vašák, M. (2000) Effect of the two conserved prolines of human growth inhibitory factor (Metallothionein-3) on its biological activity and structure fluctuation: comparison with a mutant protein. *Biochemistry* **39**, 14567–14575
73. El Ghazi, I., Martin, B. L., and Armitage, I. M. (2010) New proteins found interacting with brain metallothionein-3 are linked to secretion. *Int. J. Alzheimers Dis.* **2011**, 208634
74. Ghazi, I. E., Martin, B. L., and Armitage, I. M. (2006) Metallothionein-3 is a component of a multiprotein complex in the mouse brain. *Exp. Biol. Med.* **231**, 1500–1506
75. Meloni, G., Sonois, V., Delaine, T., Guilloureau, L., Gillet, A., Teissié, J., et al. (2008) Metal swap between Zn7-metallothionein-3 and amyloid- β -Cu protects against amyloid- β toxicity. *Nat. Chem. Biol.* **4**, 366–372
76. Cai, B., Zheng, Q., Teng, X.-C., Chen, D., Wang, Y., Wang, K.-Q., et al. (2006) The role of Thr5 in human neuron growth inhibitory factor. *J. Biol. Inorg. Chem.* **11**, 476
77. Ding, Z.-C., Teng, X.-C., Cai, B., Wang, H., Zheng, Q., Wang, Y., et al. (2006) Mutation at Glu23 eliminates the neuron growth inhibitory activity of human metallothionein-3. *Biochem. Biophys. Res. Commun.* **349**, 674–682
78. Sewell, A. K., Jensen, L. T., Erickson, J. C., Palmiter, R. D., and Winge, D. R. (1995) Bioactivity of metallothionein-3 correlates with its novel .beta. Domain sequence rather than metal binding properties. *Biochemistry* **34**, 4740–4747
79. Bousleiman, J., Pinsky, A., Ki, S., Su, A., Morozova, I., Kalachikov, S., et al. (2017) Function of metallothionein-3 in neuronal cells: do metal ions alter expression levels of MT3? *Int. J. Mol. Sci.* **18**, 1133
80. Wang, B., Wood, I. S., and Trayhurn, P. (2008) PCR arrays identify metallothionein-3 as a highly hypoxia-inducible gene in human adipocytes. *Biochem. Biophys. Res. Commun.* **368**, 88–93
81. Tanji, K., Irie, Y., Uchida, Y., Mori, F., Satoh, K., Mizushima, Y., et al. (2003) Expression of metallothionein-III induced by hypoxia attenuates hypoxia-induced cell death *in vitro*. *Brain Res.* **976**, 125–129
82. Felizola, S. J., Nakamura, Y., Arata, Y., Ise, K., Satoh, F., Rainey, W. E., et al. (2014) Metallothionein-3 (MT-3) in the human adrenal cortex and its disorders. *Endocr. Pathol.* **25**, 229–235
83. Kmiecik, A. M., Pula, B., Suchanski, J., Olbromski, M., Gomulkiewicz, A., Owczarek, T., et al. (2015) Metallothionein-3 increases triple-negative breast cancer cell invasiveness *via* induction of metalloproteinase expression. *PLoS One* **10**, e0124865
84. Merlos Rodrigo, M. A., Michalkova, H., Smidova, V., Casar, B., Rios, V. d. L., Casal, J. I., et al. (2021) MO38-2 Metallothionein-3: potential therapeutic target for sorafenib resistance in hepatocellular carcinoma. *Ann. Oncol.* **32**, S323
85. Tsuruma, K., Shimazaki, H., Ohno, Y., Inoue, Y., Honda, A., Imai, S., et al. (2012) Metallothionein-III deficiency exacerbates light-induced retinal degeneration. *Invest. Ophthalmol. Vis. Sci.* **53**, 7896–7903
86. Rodrigo, M. A. M., Michalkova, H., Strmiska, V., Casar, B., Crespo, P., de Los Rios, V., et al. (2021) Metallothionein-3 promotes cisplatin chemoresistance remodelling in neuroblastoma. *Sci. Rep.* **11**, 5496
87. Hoops, S., Sahle, S., Gauges, R., Lee, C., Pahle, J., Simus, N., et al. (2006) COPASI—a complex pathway simulator. *Bioinformatics* **22**, 3067–3074
88. Barshop, B. A., Wrenn, R. F., and Frieden, C. (1983) Analysis of numerical methods for computer simulation of kinetic processes: development of KINSIM—a flexible, portable system. *Anal. Biochem.* **130**, 134–145